COMPUTATIONAL INVESTIGATIONS OF THE EFFECTS OF WALL SURFACE TEMPERATURE ON A HYPERSONIC INLET ISOLATOR

Donghui WANG[1], Shiqichang WU[2], Yiqing LI[2] and Jingwei GAO[*,1]

[1]National University of Defence Technology, Changsha 410073, Hunan, P. R. China
[2]School of Aircraft Engineering, Nanchang Hangkong University, Nanchang 330000, Jiangxi, P.R. China
[*]Corresponding author, E-mail: mmjingwei@163.com

Flow and shock train development in a hypersonic inlet isolator at various wall surface temperatures (T_w) and freestream static temperatures (T_∞) were studied through numerical simulations. A nondimensional parameter T_w/T_∞ is used to characterize flow behaviors in hypersonic isolator. With the increase of T_w/T_∞, boundary layer thickness increases and boundary layer momentum thickness decreases at the entrance of isolator. Inside the isolator without the presence of backpressure, skin friction decreases with the increase of T_w/T_∞. The main cause is a lower velocity gradient near the wall at high temperature. A lower skin friction on high wall temperature results in a stronger separation with shock impingement. Under backpressure conditions, with the increase of T_w/T_∞, an upstream movement of the starting position of the shock train inside the isolator, an increase in the length of the shock train, and an increase in pressure coefficient on the wall surface are observed.

Keywords: hypersonic inlet isolator; wall surface temperature; boundary-layer thickness; shock train

1   Introduction

During flight, hypersonic aircraft are subjected to high levels of aerodynamic heating [1, 2, 3, 4]. To ensure the safe and effective functioning of an air-breathing hypersonic aircraft, strict and dependable thermal protection and management of the aircraft's body and the airflow ducts inside the propulsion system are prerequisites. An essential part of the propelling system, the hypersonic inlet isolator serves as an aerothermodynamic buffer to guarantee the combustor and inlet run continuously and steadily [5]. The isolator is subjected to significant aerodynamic heating since it is an internal duct in the propulsion system. The wall surface temperature within the isolator must be kept by the thermal management system within the temperature range that its material can tolerate [6]. Waltrup *et. al* [7] summarized an empirical equation for pressure distribution along the shock train in a circular duct in an early research on the shock train phenomenon within internal flow ducts. Furthermore, a great deal of numerical simulation and experimental research has shown that the boundary layer conditions upstream of the shock train have a significant role in determining the shape of the shock structure and the distribution of pressure downstream of the shock train. Changes in wall surface temperature in the isolator zone will impact the formation of the boundary layer due to heat transfer. The properties of the interaction between shock waves and the turbulent boundary layer will alter with a high tem-

perature gradient [6]. This will ultimately impact the shock train's flow form and mode of operation [7, 8]. Flow behavior of shock and pseudo-shock trains within isolators [9, 10, 11, 12], duct bending [13], shock oscillations in isolators [14, 15, 16, 17] of hypersonic inlets, and the back-pressure resistance of isolators [18, 19, 20] were all revealed by extensive studies. Furthermore, the impact of heat transfer in the isolator zone and wall temperature on shock train flow behavior have been studied [21, 22, 23, 24, 25]. Additionally investigated is heat transfer for flow in ducts [26, 27, 28]. A research team at RWTH Aachen University led by Olivier has thoroughly investigated this factor through wall preheating and heating in light of the significance of the impacts of wall surface temperature and heat transfer on shock trains [29, 30, 31, 32].

Conventional hypersonic wind-tunnel testing necessitate large, expensive test instruments in order to simulate real flight circumstances and generate high-temperature, high-enthalpy incoming freestreams. In wind-tunnel tests, the test-piece material must also be aerodynamically heated by air for a significant period of time in order for it to reach thermodynamic equilibrium. On the other hand, long-term hypersonic high-enthalpy wind-tunnel experiments are quite expensive. For this reason, simulating high-altitude aerothermo-dynamic flight conditions in wind tunnel experiments is challenging. Analyzing the flow behaviors and heat transfer in the isolator of hypersonic inlets depends heavily on the various turbulent flow scales, which are challenging to simultaneously calibrate within the hypersonic boundary layer.

This study examined a typical hypersonic inlet isolator using numerical modeling based on the limited test data that Olivier's research team was able to gather, given the challenge of accurately reproducing true high-altitude aerothermodynamic flight conditions in testing [29]. Using the test data gathered, the validity of numerical simulation was investigated. Numerical simulation was also used to further understand the shock train's flow behavior inside the isolator. Theoretical analysis and the numerical simulation results were then used to determine the physical process underlying how heat transfer and wall surface temperature affect shock train flow behavior in isolators. The rest of the paper is organized as follows. The physical model and the computational methods are described in Sec.2. In Sec.2, the code validation is also performed. Sec.3 discusses how wall temperature affects shock train in both backpressured and backpressure-free scenarios. In Sec.4, the main conclusions and findings are summarized.

2   Physical Model and Computational Methods

2.1   Physical Model

Figure 1 shows the geometrical configuration of the two-dimensional (2D) hypersonic inlet model. The dimensions of this model are identical with the wind-tunnel test model used by Olivier's research team [29]. The inlet was designed with a shock-on-lip Mach number of 7.7 and a total length of 0.5878 m. In addition, the length of the cowl, the distance between the lower wall surface at the entrance of the isolator and the cowl, and the width of the wind-tunnel test model were 0.2068, 0.0155, and 0.1 m, respectively. To reduce the side overflow on the compression ramp, a side plate was installed at each side of the model. A triangular-wedge blocking plug was placed at the exit of the isolator. Changes in the backpressure in the downstream combustor were simulated by moving the blocking plug back and forth. The wall temperature in the inlet test model was controllable through the heating devices installed on the compression ramp and the cowl. In our study, the central symmetrical plane of the inlet was selected as the 2D simulation domain. For the

convenience of subsequent analysis, the location of red dot at the ramp corner is marked as the origin of the coordinate system.
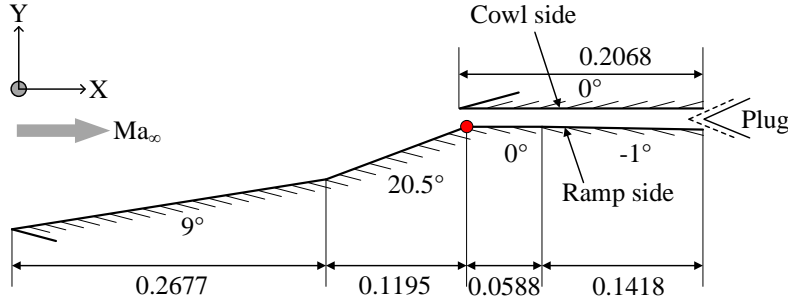

Figure 1: Schematic of two-dimensional hypersonic inlet model, units: m [29]

2.2 Computational Methods

Two-dimensional Reynolds-averaged Navier–Stokes equations were discretized using a finite volume method. The equations in integral form can be written as [33]:

$$\frac{\partial}{\partial t} \int_{\Omega} \mathbf{W} d\Omega + \oint_{\partial \Omega} (\mathbf{F}_{inv} - \mathbf{F}_{vis}) \, dS = 0, \tag{1}$$

where, Ω is the control volume, which is bounded by closed surface dS. $\mathbf{W}$, $\boldsymbol{F}_{inv}$ and $\boldsymbol{F}_{vis}$ represent the conservation variable vector, the inviscid flux vector and the viscous flux vector, respectively [33]. Inviscid convective fluxes were discretized using Roe's flux-difference splitting scheme which can be expressed as:

$$\mathbf{F}_{inv} = \frac{1}{2} \left(\mathbf{F}_{R,inv} + \mathbf{F}_{L,inv} \right) - \frac{1}{2} \Gamma |\hat{A}| \delta \mathbf{W}, \tag{2}$$

where, $\boldsymbol{F}_{R,inv}$ and $\boldsymbol{F}_{L,inv}$ are computed using the solution vectors $\boldsymbol{W_R}$ and $\boldsymbol{W_L}$ on the right and left sides of the face and $\delta \mathbf{W}$ is the spatial difference $\boldsymbol{W_R} - \boldsymbol{W_L}$. Viscous fluxes were discretized using a second-order centered difference scheme. A point implicit method was employed to advance time. The transition shear stress transport model was selected for turbulence closure. In this model, an intermittency variable χ is solved through the transport equation [34]:

$$\frac{\partial (\rho \chi)}{\partial t} + \frac{\partial (\rho u_j \chi)}{\partial x_j} = P_{\chi 1} - E_{\chi 1} + P_{\chi 2} - E_{\chi 2} + \frac{\partial}{\partial x_j} \left[\left(\mu + \frac{\mu_t}{\sigma_\chi} \right) \frac{\partial \chi}{\partial x_j} \right]. \tag{3}$$

The transition source terms are defined as follows:

$$P_{\chi 1} = C_{a1} F_{length} \rho \mathbf{S} \left(\chi F_{onset} \right)^{C_{\chi 3}}, \quad E_{\chi 1} = C_{e1} P_{\chi 1} \chi, \tag{4}$$

where $\boldsymbol{S}$ is the strain rate magnitude, F_{length} is an empirical correlation that controls the length of the transition region. The destruction source terms are defined as follows:

$$P_{\chi 2} = C_{a2} \rho \boldsymbol{\Omega} \chi F_{turb}, \quad E_{\chi 2} = C_{e2} P_{\chi 2} \chi, \tag{5}$$

where Ω is the vorticity magnitude. The transition onset is controlled by the following functions:

$$Re_v = \frac{\rho y^2 S}{\mu}, \tag{6}$$

$$R_T = \frac{\rho k}{\mu \omega}, \tag{7}$$

$$F_{\text{onset 1}} = \frac{Re_v}{2.193 Re_{\theta c}}, \tag{8}$$

$$F_{\text{onset 2}} = \min\left(\max\left(F_{\text{onset 1}}, F_{\text{onset 1}}^4\right), 2.0\right), \tag{9}$$

$$F_{\text{onset 3}} = \max\left(1 - \left(\frac{R_T}{2.5}\right)^3, 0\right), \tag{10}$$

$$F_{\text{onset}} = \max\left(F_{\text{onset 2}} - F_{\text{onset 3}}, 0\right), \tag{11}$$

$$F_{\text{turb}} = e^{-\left(\frac{R_T}{4}\right)^4}. \tag{12}$$

$Re_{\theta c}$ is the critical Reynolds number where the intermittency first starts to increase in the boundary layer. The model constants are:

$$C_{a1} = 2, \quad C_{e1} = 1, \quad C_{a2} = 0.06, \quad C_{e2} = 50, \quad C_{\chi 3} = 0.5, \quad \sigma_\chi = 1. \tag{13}$$

The specific heat of air is calculated by polynomial fitting [35]. High temperature air dissociation and ionization are not considered in current study. The present analysis does not consider the impacts of convective and radiative heat transmission since they are deemed to be less significant in the hypersonic forebody region compared to the isolator. In solving the equations, a in-house developed solver is used to perform numerical simulations.

Figure 2 shows the an example mesh generated for the hypersonic inlet as well as the computational domain. The computational domain was completely covered by a structured mesh. To accurately capture the flow behavior in the near-wall regions, the thickness y of the first mesh layer for the near-wall regions of the compression ramp and the cowl was set to less than 1×10^{-5} m. The pressure farfield boundary conditions are applied to specify the freestream static temperature, static pressure and $Mach$ number. Pressure outlet-A are specified with static temperature and static pressure identical with freestream condition. For non backpressure situations, the static pressure for boundary pressure outlet-B is assigned with the freestream static pressure. For backpressure situations, the static pressure is larger than the freestream static pressure allowing the generation of shock train within the isolator.
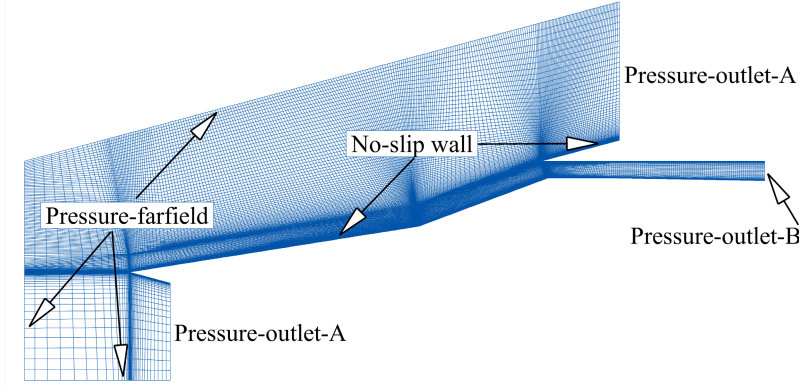
Figure 2: Example hypersonic inlet mesh and computational domain.

2.3 Code validation

Three sets of mesh are generated for grid convergence study. The cell number for coarse, medium and dense meshes are 143800, 380000 and 635000, respectively. The maximum y^+ value of the first layer mesh near wall for three sets of meshes are 1.5, 0.6 and 0.3, respectively. The simulation parameters are given in Tab. 1. As shown in Fig.3, the pressure coefficient distributions obtained by medium and dense mesh nearly overlap with each and those results fit the experimental data [29] much better than those obtained by coarse mesh. To balance simulation accuracy and computational cost, medium mesh is selected for subsequent study. It is found that the sudden rise location of pressure coefficients on the cowl side is captured by numerical simulations. After the expansion waves, the experimental pressure coefficients are slightly higher than the numerical values. On the ramp side before the first expansion wave, the experimental pressure coefficients are in good agreement with the numerical values. The discrepancy between experimental data and numerical simulations on the cowl side might result from the three-dimensional effects in which side wall-induced compression waves interact with cowl shock waves, whereas side wall-induced compression waves are not considered in two-dimensional simulations.

Table 1: Simulation parameters for code validation.

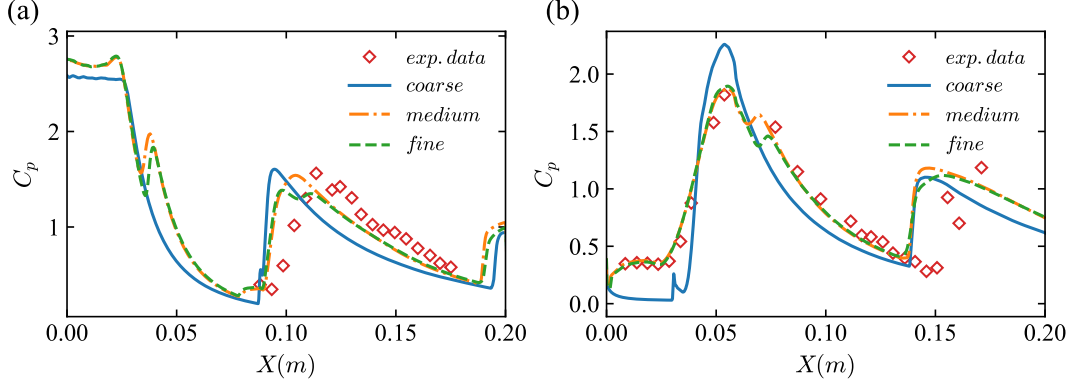| Ma_∞	T_∞ (K)	p_∞ (Pa)	U_∞ (m/s)	$Re_{\infty,1}$ $(10^6/m)$
7.7	125	750	1745	4.1

5

Figure 3: Pressure coefficient C_p ($C_p = p/\frac{1}{2}\rho_\infty U_\infty^2$) distributions on isolator wall surface: (a) Cowl side. (b) Ramp side. Experimental data from [29].

3 Results and Discussions

3.1 Effects of wall temperature without backpressure

To analyze the effects of wall surface temperature flow behavior inside the isolator without backpressure, four cases are simulated under the same freestream condition. The specifications of simulation parameters are given in Tab. 2. Here, the parameter $Re_{\infty,st} = (\rho_\infty U_\infty x)/\mu_\infty$ is the Reynolds number based on freestream density, velocity, viscosity and the starting distance x. The starting distance x is the boundary layer development distance along inlet compression ramp at the entrance of isolator. In our study, $x = 0.3986$ m. Figure 4 shows the density gradient ($|\nabla\rho| = \sqrt{(\partial\rho/\partial x)^2 + (\partial\rho/\partial y)^2}$) contours inside the isolator at

Table 2: Simulation parameters for cases $C-1 \sim C-4$.

Case No.	Ma_∞	T_∞ (K)	p_∞ (Pa)	T_w (K)	T_w/T_∞	$Re_{\infty,st}$ $(10^6/m)$
C-1	7.7	125	750	300	2.4	1.5
C-2	7.7	125	750	600	4.8	1.5
C-3	7.7	125	750	800	6.4	1.5
C-4	7.7	125	750	1000	8.0	1.5

various wall surface temperatures T_w. As shown in the figure, the flow field inside the isolator exhibited basically the same structure at various T_w values. The cowl-induced incident shock wave and the expansion wave generated at the point of inflection of the compression ramp intersected at the entrance of the isolator. As T_w increased from 300 to 1000 K, there is a slight decrease in the length of the reflected shock wave. As shown at the point of intersection (at approximately X = 0.13 m) between the shock and the compression ramp as well as the point of intersection (at approximately X = 0.18 m) between the shock and the cowl, an increase in T_w led to a slight upstream movement of the point of intersection between the shock wave and the wall surface. The separation region caused by the event shock impinging on the ramp grows in size as wall temperature rises. The reason for this is because when wall temperature rises, boundary layer thickness also rises. This decreases the boundary layer's capacity to withstand reverse pressure gradients, enlarging the separation zone.
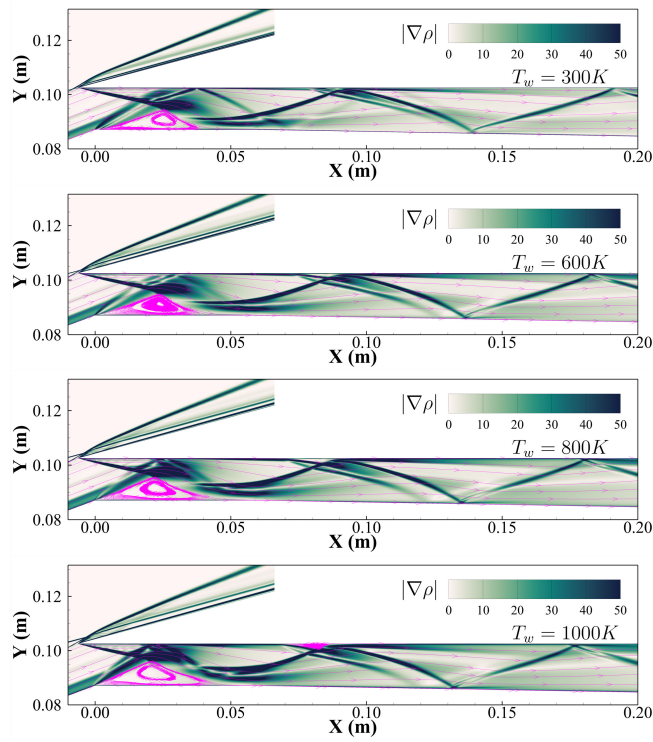
Figure 4: Density gradient ($|\nabla\rho| = \sqrt{(\partial\rho/\partial x)^2 + (\partial\rho/\partial y)^2}$) contours inside the isolator for cases $C-1$, $C-2$, $C-3$ and $C-4$ without backpressure. The corresponding wall surface temperature T_w are $300K$, $600K$, $800K$ and $1000K$, respectively.

Figure 5 shows the kinetic energy ratio $\rho U^2/\rho_\infty U_\infty^2$ perpendicular to ramp wall at various X locations in the isolator for cases $C-1 \sim C-4$. Here, H_x represents the isolator height at location X. The five profiles from (a) to (e) are extracted at X locations 0.0 m, 0.05 m, 0.10 m, 0.15 m and 0.20 m, respectively. It is shown that with the increase of T_w/T_∞, the kinetic ratio at a given Y location decreases. This observation suggests that the increase of wall temperature can decrease the kinetic energy in boundary layer.
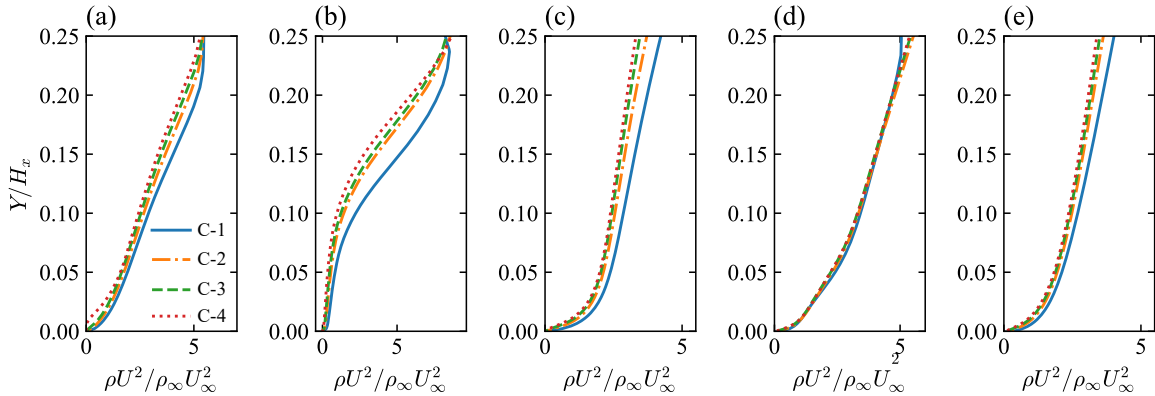

Figure 5: Kinetic energy ratio $\rho U^2/\rho_\infty U_\infty^2$ perpendicular to ramp wall at various X locations in the isolator for cases $C-1 \sim C-4$: (a) $X = 0.0\,m$. (b) $X = 0.05\,m$ (c) $X = 0.10\,m$ (d) $X = 0.15\,m$. (e) $X = 0.20\,m$.

Figure 6 shows the static pressure coefficient C_p distribution along the wall surface inside the isolator at

various T_w values for cases $C-1 \sim C-4$ ($X = 0\ m$ corresponds to the point of inflection of the compression ramp at the entrance of the isolator). The lines show the numerical simulation results and the symbols show the experimental data obtained by Olivier's research team [29]. As shown in Fig. 6, the pressure coefficient on the cowl side wall surface at the starting location of the sudden rise was consistent with the test data. After the expansion waves, the measured values of C_p are slightly higher than the simulated values. On the compression ramp side wall surface, before the first expansion wave, the measured values of C_p are in good agreement with the simulated data. The starting position of the second shock wave was found to be closer to the upstream region in the numerical simulation than in the test. This may be because this position is the starting position of multiple compression wave systems in the test, whereas it is the starting position of only one shock wave in the numerical simulation [29]. At the same location on the X axis, the measured value of C_p was higher at $T_w = 600\ K$ than at $T_w = 300\ K$. A similar trend is found in the numerical simulation results. Corresponding to Fig. 4, it can be seen from Fig. 6 that the point of incidence of shock waves on the wall surface on the cowl and the compression ramp sides moved upstream as T_w increased. As demonstrated in Fig. 6 (a), at T_w=800 and 1000 K, due to its exposure to expansion waves first, the pressure coefficient on the cowl side wall surface at approximately $X = 0.02\ m$ suddenly increased and then decreased. At T_w=300 and 600 K, the pressure coefficient on the cowl side wall surface at the corresponding location first decreased to a small extent and then increased. These fluctuations in pressure coefficient demonstrate that the difference in T_w resulted in changes in the flow field structure of the cowl induced incident shock waves and the compression ramp induced expansion waves near the intersection region. This was ultimately reflected by changes in the wave system incident on the cowl side wall surface. As demonstrated in Fig. 6 (b), the higher T_w is, the higher the pressure coefficient on the compression ramp side wall surface at the same location on the X axis within the range of $0 \sim 0.06\ m$ is. The maximum peak pressure on the wall surface occurred at X=0.06 m and T_w=1000 K.
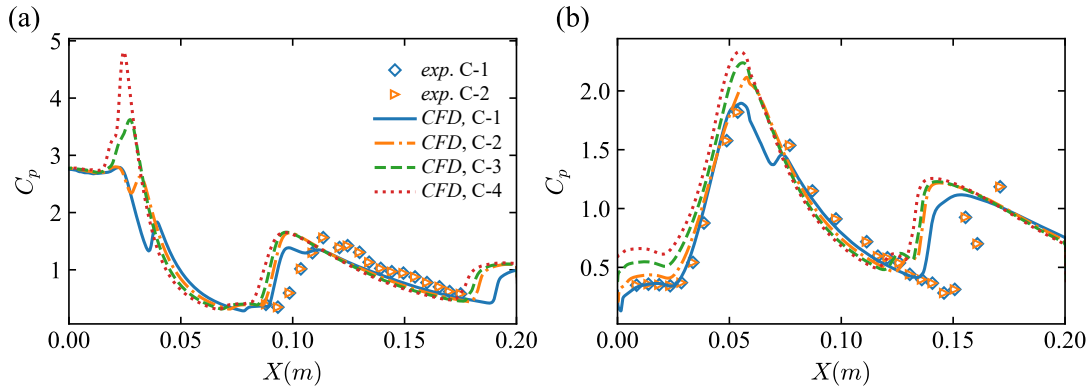

Figure 6: Pressure coefficient C_p ($C_p = p/\frac{1}{2}\rho_\infty U_\infty^2$) distributions on isolator wall surface for cases $C-1 \sim C-4$: (a) Cowl side. (b) Ramp side. Experimental data from [29].

Figure 7 shows the skin friction coefficient C_f distribution along the wall surface inside the isolator at various T_w values for cases $C-1 \sim C-4$. Here $C_f = \tau/\frac{1}{2}\rho_\infty U_\infty^2$ and τ is the wall shear stress. It is shown that for skin friction coefficient on cowl side, the C_f values are greatly interfered by shock-boundary layer interaction at $X < 0.1\ m$. The effects of wall temperature on C_f values can be clearly observed at $X > 0.1$

m. It is found that C_f increases with the decrease of T_w/T_∞. On ramp side, larger C_f value can be found in most portion of isolator wall surface with smaller T_w/T_∞ (case $C-1$).
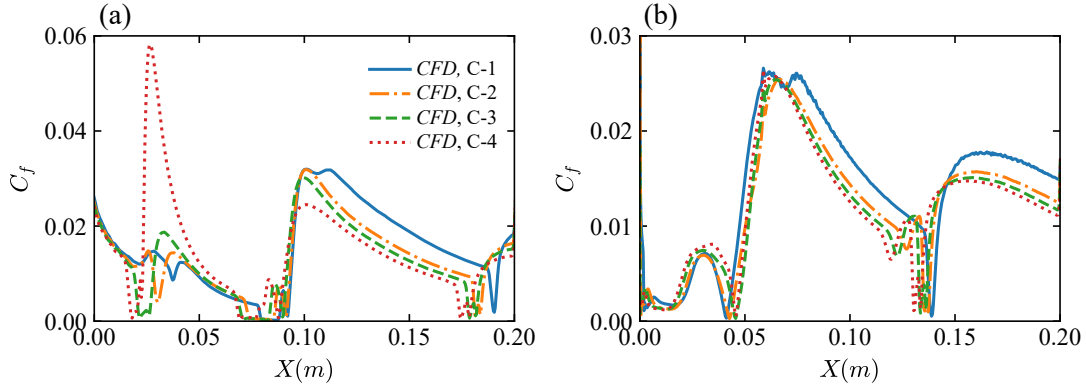

Figure 7: Skin friction coefficient C_f ($C_f = \tau/\frac{1}{2}\rho_\infty U_\infty^2$) distributions on isolator wall surface for cases $C-1 \sim C-4$: (a) Cowl side. (b) Ramp side.

To further analyze the influence wall surface temperature effects on isolator, we performed simulations with fixed wall surface temperature under different freestream with various static temperature. The simulation parameters for cases $C-5 \sim C-8$ are given in Tab.3. Figure 8 shows the kinetic energy ratio

Table 3: Simulation parameters for cases $C-5 \sim C-8$.

Case No.	Ma_∞	T_∞ (K)	p_∞ (Pa)	T_w (K)	T_w/T_∞	$Re_{\infty,st}$ ($10^6/m$)
C-5	7.4	84	2000	1000	11.9	7.5
C-6	7.4	122	2000	1000	8.2	4.3
C-7	7.4	160	2000	1000	6.3	2.9
C-8	7.4	250	2000	1000	4.0	1.6

$\rho U^2/\rho_\infty U_\infty^2$ perpendicular to ramp wall at various X locations in the isolator for cases $C-5 \sim C-8$. The X locations are identical with values in Fig.5. It is shown that with the increase of T_w/T_∞, the kinetic ratio at a given Y location decreases. This observation is consistent with results found in Fig.5.
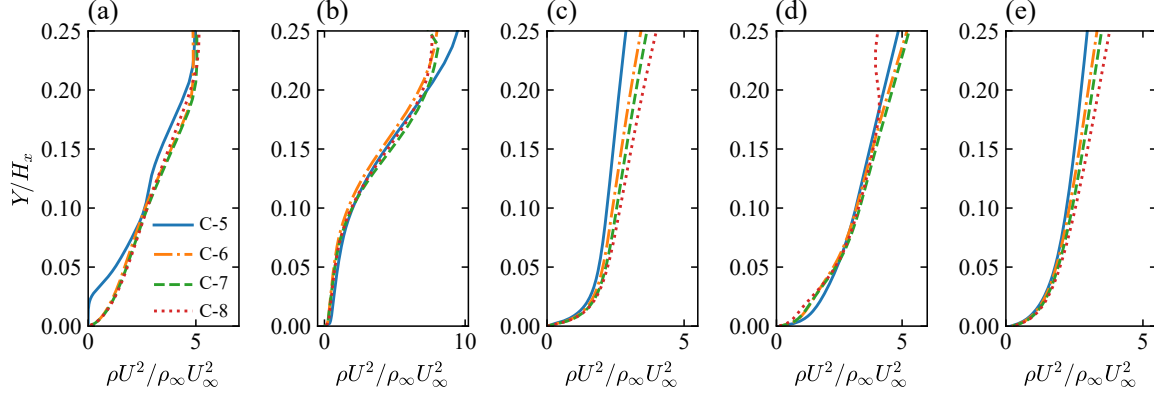
9

Figure 8: Kinetic energy ratio $\rho U^2/\rho_\infty U_\infty^2$ perpendicular to ramp wall at various X locations in the isolator for cases $C-5 \sim C-8$: (a) $X = 0.0\ m$. (b) $X = 0.05\ m$ (c) $X = 0.10\ m$ (d) $X = 0.15\ m$. (e) $X = 0.20\ m$.

Figure 9 shows the pressure coefficient C_p distribution on the wall surface inside the isolator without backpressure for cases $C-5 \sim C-8$. As shown in Fig. 9, at T_∞=250 K (case $C-5$), the simulated and measured values were in good agreement. The effects of wall surface temperature on the flow behavior of the airflow inside the isolator at a fixed T_w are similar to those of T_w under fixed incoming freestream conditions. Of the four cases differing in T_∞, the pressure coefficient on the wall surface was higher at T_∞=84 K than at other T_∞ values.

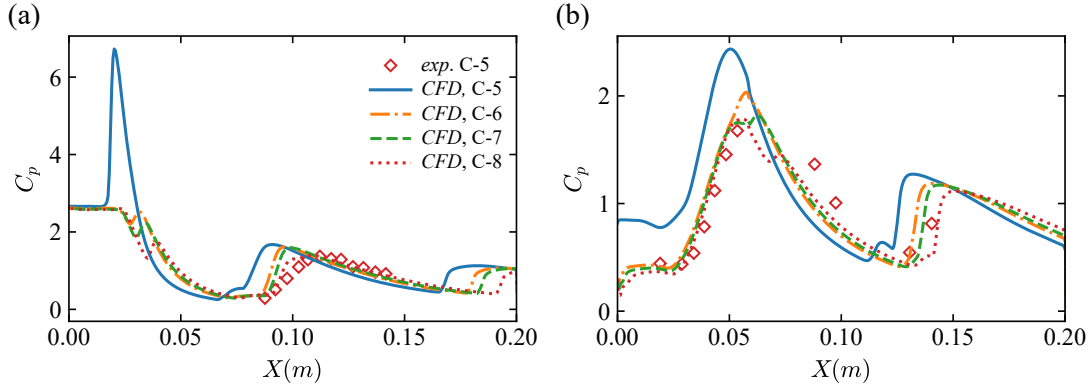**Figure 9: Pressure coefficient C_p ($C_p = p/\frac{1}{2}\rho_\infty U_\infty^2$) distributions on isolator wall surface for cases $C-5 \sim C-8$: (a) Cowl side. (b) Ramp side. Experimental data from [29].**

Figure 10 shows the skin friction coefficient C_f distribution along the wall surface inside the isolator at various T_w values for cases $C-5 \sim C-8$. It is observed that for skin friction coefficient on cowl side, the C_f values are greatly interfered by shock-boundary layer interaction at $X < 0.1\ m$. The effects of wall temperature on C_f values can be clearly observed at $X > 0.1\ m$. It is found that C_f increases with the decrease of T_w/T_∞. On ramp side, larger C_f value can be found in most portion of isolator wall surface with smaller T_w/T_∞. The above observations are consistent with the results found in Fig.7.
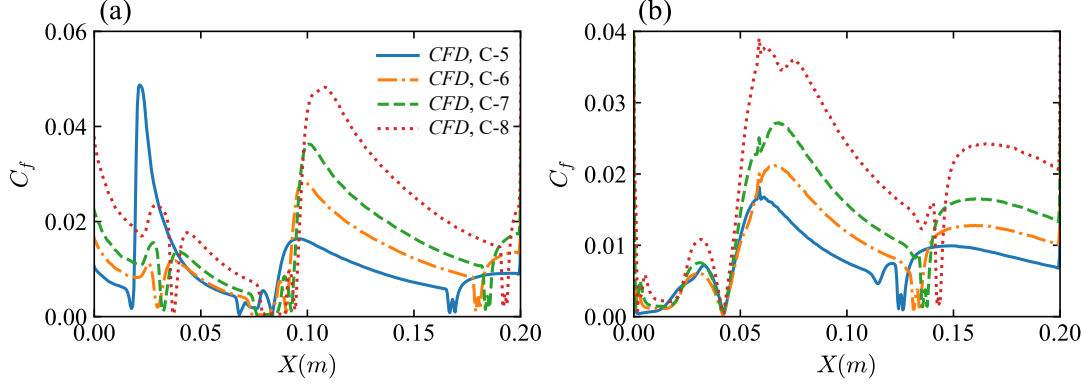
10

Figure 10: Skin friction coefficient C_f ($C_f = \tau / \frac{1}{2} \rho_\infty U_\infty^2$) distributions on isolator wall surface for cases $C-5 \sim C-8$: (a) Cowl side. (b) Ramp side.

With the above analysis, we find that heat transfer in boundary layer greatly influences flow behavior in hypersonic isolator. Hirschel [36] suggested an empirical relation to estimate the boundary layer thickness considering wall and freestream temperature:

$$\delta_x = 0.37 \frac{st}{(Re_{\infty,st})^{0.2}} \left(\frac{T_w}{T_\infty} \right)^{(1+\omega)}, \tag{14}$$

here, st is the boundary layer development distance. We denote st is the compression surface length before the entrance of isolator and thus $st = 0.3986\ m$. ω=1 is suggested [36]. For compression ramp in current study, it is found that $\omega = -0.7 \sim -0.6$. Figure 11 shows the variation of boundary layer thickness with T_w/T_∞ for both numerical simulations of cases $C-1 \sim C-8$ and the results obtained by Eq. 14 (denoted as 'ANA' in legend). It is shown that with the increase of T_w/T_∞, the boundary layer thickness increases. The deviation of numerical results and the empirical prediction might result from the fact that the empirical relation is developed upon flat plate while the boundary layer development on compression ramp is affected by shock waves. The trend of variations between numerical simulation data and the analytical prediction is close. The results indicate that for a given freestream condition, the higher wall surface temperature leads to an increase of boundary layer thickness.
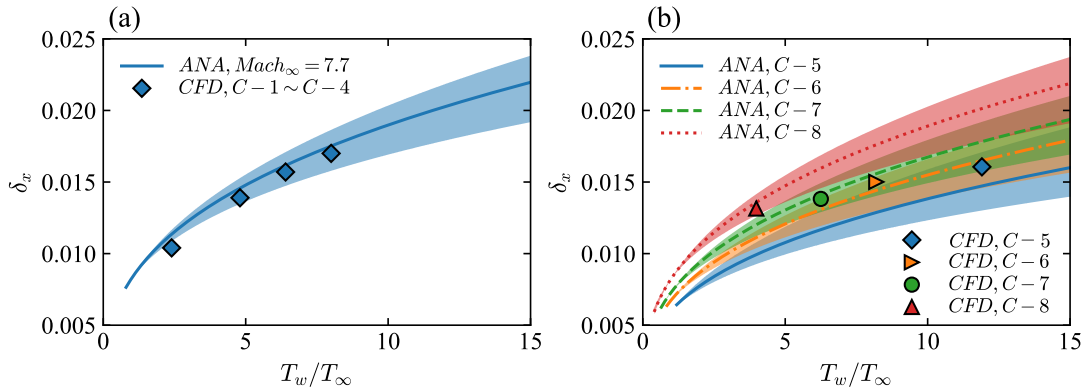

Figure 11: Boundary layer thickness at the isolator entrance δ_x with the development distance $x = 0.3986\ m$: (a) Ma_∞=7.7. (b) Ma_∞=7.4.

11

3.2 Effects of wall temperature under backpressure conditions

Shock train formation inside an isolator requires a high downstream backpressure. Therefore, it is necessary to examine the effects of wall surface temperature on the airflow inside the isolator under high downstream backpressure conditions. Figure 12 shows the density gradient contours in the hypersonic inlet isolator in the presence of an incoming freestream with a Mach number of 7.7 under a back-pressure 270 times the p_∞ of the incoming freestream. As demonstrated in Fig. 12, the shock train inside the isolator was distributed in an asymmetric manner. The starting point of the shock train is located at approximately X=0.08 m. On the compression ramp side wall surface, the starting position of the shock train is marked by an oblique shock wave. Shock nodes with alternating shock and expansion waves were located primarily near the cowl side wall surface inside the isolator. At T_w=300 K, shock nodes with alternating shock and expansion waves were located in the core flow region inside the isolator. At other T_w values, shock nodes were close to the cowl-side wall surface.
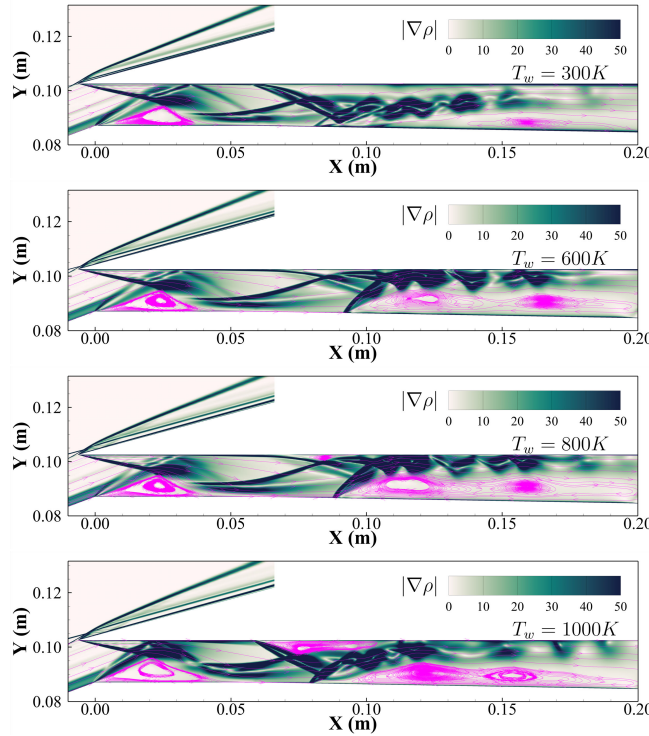

Figure 12: Density gradient ($|\nabla\rho| = \sqrt{(\partial\rho/\partial x)^2 + (\partial\rho/\partial y)^2}$) contours inside the isolator for cases $C-1$, $C-2$, $C-3$ and $C-4$ under backpressure. The corresponding wall surface temperature T_w are $300K$, $600K$, $800K$ and $1000K$, respectively.

Figure 13 shows the pressure coefficient distribution along the inner wall ramp insides the isolator for cases $C-1 \sim C-8$. As shown in Fig.13 (a), for Ma_∞=7.7, the backpressure is 270 times the freestream static pressure. While for Ma_∞=7.4 as shown in Fig.13 (b), the backpressure is 200 times the freestream static pressure. It is observed that in the region upstream of the starting position of the shock train, the pressure coefficient distribution on the ramp side wall surface under backpressure conditions is basically consistent with that without backpressure conditions. Within the shock-train region, an increase in T_w/T_∞

led to an increase in pressure coefficient on the ramp wall surface and an upstream movement of the starting position of the shock train.
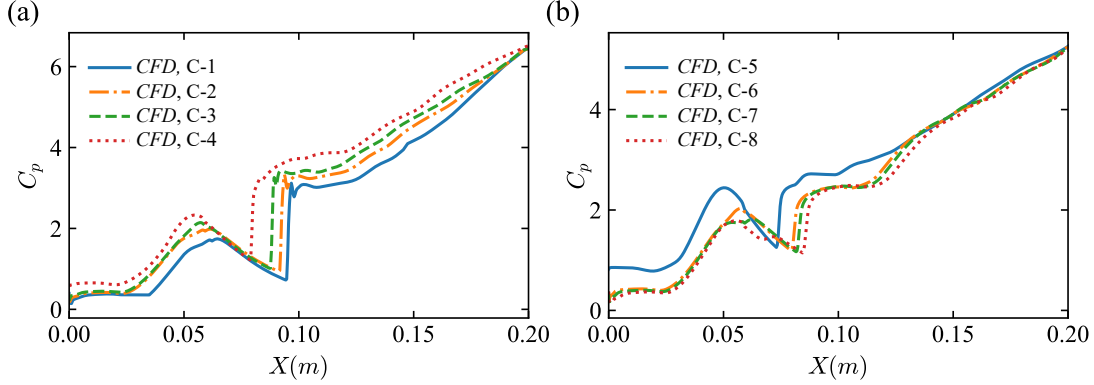

Figure 13: Pressure coefficient C_p ($C_p = p/\frac{1}{2}\rho_\infty U_\infty^2$) distributions on isolator ramp wall surface for cases $C-1 \sim C-8$: (a) Ma_∞=7.7. (b) Ma_∞=7.4.

Hirschel [36] suggested an empirical relation to estimate the boundary layer momentum thickness considering wall and freestream temperature:

$$\theta_x = 0.036 \frac{st}{(Re_{\infty,st})^{0.2}} \left(\frac{T_w}{T_\infty}\right)^{0.2(\omega-4)}. \tag{15}$$

Figure 14 shows the variation of boundary layer momentum thickness with T_w/T_∞ for both numerical simulations of cases $C-1 \sim C-8$ and the results obtained by Eq. 15 (denoted as 'ANA' in legend). It is shown that with the increase of T_w/T_∞, the boundary layer momentum thickness decreases. For a given freestream condition, the higher wall surface temperature leads to the decrease of boundary layer momentum thickness.
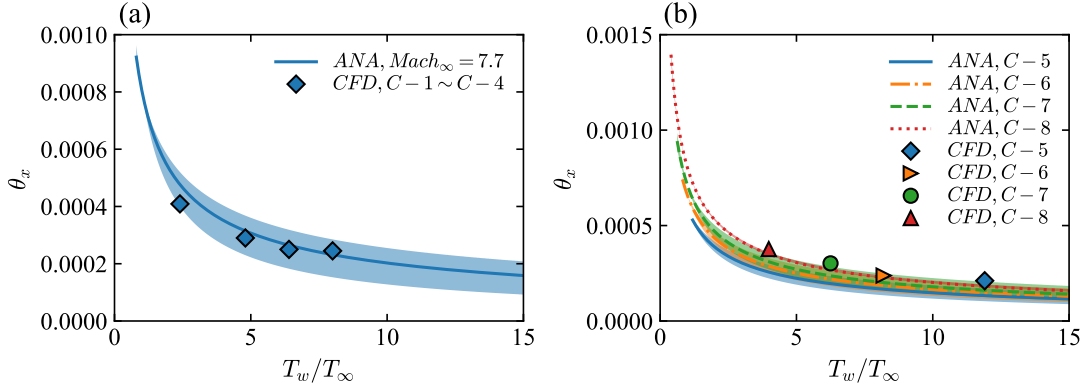

Figure 14: Boundary layer momentum thickness at the isolator entrance θ_x with the development distance $x = 0.3986\,m$: (a) Ma_∞=7.7. (b) Ma_∞=7.4.

4   Conclusions

The following conclusions can be obtained from this study:

13

First, the flow in a hypersonic inlet isolator at different wall surface temperatures and freestream static temperatures can be accurately simulated by the two-dimensional stable Reynolds-averaging numerical approach that is employed. The test data and the simulated pressure coefficient distribution were found to be in agreement. This implies the validity of the numerical approach.

Second, for the purpose of characterizing the flow behaviors in the hypersonic isolator, the nondimensional parameter T_w/T_∞ is crucial. Boundary layer thickness rises and boundary layer momentum thickness falls when T_w/T_∞ grows. The skin friction reduces when T_w/T_∞ increases. The primary reason is a reduced velocity gradient at high temperature close to the wall. With shock impingement, a stronger separation is produced by a reduced skin friction on a high wall temperature.

Third, under backpressure conditions, with the increase of T_w/T_∞, an upstream movement of the starting position of the shock train inside the isolator, an increase in the length of the shock train, and an increase in pressure coefficient on the wall surface are observed.

Acknowledgement

Nomenclature

Ma_∞	Freestream Mach number
T_w	wall temperature
T_∞	Freestream static temperature
p_∞	Freestream static pressure
δ	Boundary layer thickness
θ	Boundary layer momentum thickness
Re_θ	Reynolds number based on boundary layer momentum thickness
C_p	Pressure coefficient
C_f	Skin friction coefficient

References

[1] Quan Han, Chengdong Sun, Yi Tao, Zhongwu Li, Yan Zhang, and Yunfei Chen. Thermal protection of a hypersonic vehicle by modulating stagnation-point heat flux. *Aerospace Science and Technology*, 98:105673, 2020.

[2] Diego Exposito and Zeeshan A. Rana. Computational investigations into heat transfer over a double wedge in hypersonic flows. *Aerospace Science and Technology*, 92:839–846, 2019.

[3] Tongqing Guo, Ennan Shen, Zhiliang Lu, Di Zhou, and Jiangpeng Wu. Thermal flutter prediction at trajectory points of a hypersonic vehicle based on aerothermal synchronization algorithm. *Aerospace Science and Technology*, 94:105381, 2019.

[4] Liang Zhu, Xiong Chen, Xiaotao Tian, Jun Song, Hao Li, and Shan Sun. Assessment on jet direction effect on drag and heat reduction efficiency for hypersonic vehicles. *Aerospace Science and Technology*, 106:105932, 2020.

[5] Jack J. McNamara and Peretz P. Friedmann. Aeroelastic and aerothermoelastic analysis in hypersonic flow: Past, present, and future. *AIAA Journal*, 49(6):1089–1122, 2011.

[6] Robert F. Cuffel and Lloyd H. Back. Flow and heat transfer measurements in a pseudo-shock region with surface cooling. *AIAA Journal*, 14(12):1716–1722, 1976.

[7] P. J. Waltrup and F. S. Billig. Structure of shock waves in cylindrical ducts. *AIAA Journal*, 11(10):1404–1408, 1973.

[8] Kazuyasu Matsuo, Yoshiaki Miyazato, and Heuy-Dong Kim. Shock train and pseudo-shock phenomena in internal gas flows. *Progress in Aerospace Sciences*, 35(1):33–100, 1999.

[9] Brandon Morgan, Karthik Duraisamy, and Sanjiva K. Lele. Large-eddy simulations of a normal shock train in a constant-area isolator. *AIAA Journal*, 52(3):539–558, 2014.

[10] Heeseok Koo and Venkatramanan Raman. Large-eddy simulation of a supersonic inlet-isolator. *AIAA Journal*, 50(7):1596–1613, 2012.

[11] J. L. Wagner, K. B. Yuceil, A. Valdivia, N. T. Clemens, and D. S. Dolling. Experimental investigation of unstart in an inlet / isolator model in mach 5 flow. *AIAA Journal*, 47(6):1528–1542, 2009.

[12] Christian Fischer and Herbert Olivier. *Experimental Investigation of the Internal Flow Field of a Scramjet Engine*.

[13] Hui-jun Tan and Shu Sun. Preliminary study of shock train in a curved variable-section diffuser. *Journal of Propulsion and Power*, 24(2):245–252, 2008.

[14] Wei-Yi Su and Kun-Yuan Zhang. Back-pressure effects on the hypersonic inlet-isolator pseudoshock motions. *Journal of Propulsion and Power*, 29(6):1391–1399, 2013.

[15] Hui-Jun Tan, Shu Sun, and Zhi-Long Yin. Oscillatory flows of rectangular hypersonic inlet unstart caused by downstream mass-flow choking. *Journal of Propulsion and Power*, 25(1):138–147, 2009.

[16] Wenxin Hou, Juntao Chang, Youyin Wang, Chen Kong, and Wen Bao. Experimental study on the forced oscillation of shock train in an isolator with background waves. *Aerospace Science and Technology*, 106:106129, 2020.

[17] Amjad A. Pasha, Khalid A. Juhany, and Subramania N. Pillai. One-equation turbulence models applied to practical scramjet inlet. *International Journal of Turbo & Jet-Engines*, page 000010151520210013, 2021.

[18] Hu Ren, Huacheng Yuan, Jinsheng Zhang, and Binqian Zhang. Experimental and numerical investigation of isolator in three-dimensional inward turning inlet. *Aerospace Science and Technology*, 95:105435, 2019.

[19] Xianzong Meng, Zhengyin Ye, Zheng Hong, and Kun Ye. Impacts of panel vibration on shock train structures and performance of two-dimensional isolators. *Aerospace Science and Technology*, 104:105978, 2020.

[20] Zhufei Li, Wenzhi Gao, Hongliang Jiang, and Jiming Yang. Unsteady behaviors of a hypersonic inlet caused by throttling in shock tunnel. *AIAA Journal*, 51(10):2485–2492, 2013.

[21] L. Brown, C. Fischer, R.R. Boyce, B. Reinartz, and H. Olivier. Computational studies of the effect of wall temperature on hypersonic shock-induced boundary layer separation. In Klaus Hannemann and Friedrich Seiler, editors, *Shock Waves*, pages 1231–1236, Berlin, Heidelberg, 2009. Springer Berlin Heidelberg.

[22] Lianjie Yue, Hongbo Lu, Yabin Xiao, Lihong Chen, and Xinyu Chang. Role of wall temperature on shock train in a rectangular isolator. In Gabi Ben-Dor, Oren Sadot, and Ozer Igra, editors, *30th International Symposium on Shock Waves 1*, pages 425–430, Cham, 2017. Springer International Publishing.

[23] Chenlin Zhang, Juntao Chang, MengMeng Liu, Shuo Feng, Wen Shi, and Wen Bao. Effect of heat release on movement characteristics of shock train in an isolator. *Acta Astronautica*, 133:185–194, 2017.

[24] Guillermo Araya, Christian J. Lagares, Jean Santiago, and Kenneth E. Jansen. Wall temperature effect on hypersonic turbulent boundary layers via dns. In *AIAA Scitech 2021 Forum*, VIRTUAL EVENT, 2021. American Institute of Aeronautics and Astronautics.

[25] Ke Zhu, Lu-Xin Jiang, Wei-Dong Liu, Ming-Bo Sun, Qian-Cheng Wang, and Zhi-Wei Hu. Wall temperature effects on shock wave/turbulent boundary layer interaction via direct numerical simulation. *Acta Astronautica*, 178:499–510, 2021.

[26] Hayder I. Mohammed, Pouyan T. sardari, and Donald Giddings. Multiphase flow and boiling heat transfer modelling of nanofluids in horizontal tubes embedded in a metal foam. *International Journal of Thermal Sciences*, 146:106099, 2019.

[27] C.J. Ho, Yen-Chung Liu, Mohammad Ghalambaz, and Wei-Mon Yan. Forced convection heat transfer of nano-encapsulated phase change material (nepcm) suspension in a mini-channel heatsink. *International Journal of Heat and Mass Transfer*, 155:119858, 2020.

[28] Liang-Han Chien, Yi-Ting Cheng, Ying-Liang Lai, Wei-Mon Yan, and Mohammad Ghalambaz. Experimental and numerical study on convective boiling in a staggered array of micro pin-fin microgap. *International Journal of Heat and Mass Transfer*, 149:119203, 2020.

[29] Christian Fischer and Herbert Olivier. Experimental investigation of the shock train in an isolator of a scramjet inlet. In *17th AIAA International Space Planes and Hypersonic Systems and Technologies Conference*, San Francisco, California, U.S.A., 2011. American Institute of Aeronautics and Astronautics.

[30] C. Fischer and H. Olivier. Experimental investigation of wall and total temperature influence on a shock train. *AIAA Journal*, 52(4):757–766, 2014.

[31] Zhitan Zhou, Xiaoyang Liang, Changfang Zhao, Guigao Le, and Yifu Ding. Investigations of base thermal environment on four-nozzle liquid launch vehicle at high altitude. *Journal of Spacecraft and Rockets*, 57(1):49–57, 2020.

[32] Kuo-Cheng Lin, Chung-Jen Tam, Dean Eklund, Kevin Jackson, and Thomas Jackson. *Effects of Temperature and Heat Transfer on Shock Train Structures inside Constant-Area Isolators*.

[33] Yang Zhang, Laiping Zhang, Xin He, Xiaogang Deng, and Haisheng Sun. Detached eddy simulation of complex separation flows over a modern fighter model at high angle of attack. *Communications in Computational Physics*, 22(5):1309–1332, 2017.

[34] Nicholas Georgiadis and Dennis Yoder. Recalibration of the shear stress transport model to improve calculation of shock separated flows. In *51st AIAA Aerospace Sciences Meeting including the New Horizons Forum and Aerospace Exposition*, Grapevine (Dallas/Ft. Worth Region), Texas, 2013. American Institute of Aeronautics and Astronautics.

[35] Alexander Burcat and Branko Ruscic. Third millennium ideal gas and condensed phase thermochemical database for combustion with updates from active thermochemical tables. Technical Report ANL-05/20, Argonne National Lab, 2005.

[36] E. H. Hirschel. *Basics of Aerothermodynamics*. Springer-Verlag Berlin, Heidelberg, 2005.